

Computations of Flow Field and Heat Transfer in a Stator Vane Passage Using the $\overline{v^2-f}$ Turbulence Model

A. Sveningsson¹

e-mail: andreas.sveningsson@chalmers.se

L. Davidson

Division of Thermo and Fluid Dynamics,
Department of Mechanical Engineering,
Chalmers University of Technology,
SE-412 96, Gothenburg, Sweden

In this study three-dimensional simulations of a stator vane passage flow have been performed using the $\overline{v^2-f}$ turbulence model. Both an in-house code (CALC-BFC) and the commercial software FLUENT are used. The main objective is to investigate the $\overline{v^2-f}$ model's ability to predict the secondary fluid motion in the passage and its influence on the heat transfer to the end walls between two stator vanes. Results of two versions of the $\overline{v^2-f}$ model are presented and compared to detailed mean flow field, turbulence, and heat transfer measurements. The performance of the $\overline{v^2-f}$ model is also compared with other eddy-viscosity-based turbulence models, including a version of the $\overline{v^2-f}$ model, available in FLUENT. The importance of preventing unphysical growth of turbulence kinetic energy in stator vane flows, here by use of the realizability constraint, is illustrated. It is also shown that the $\overline{v^2-f}$ model predictions of the vane passage flow agree well with experiments and that, among the eddy-viscosity closures investigated, the $\overline{v^2-f}$ model, in general, performs the best. Good agreement between the two different implementations of the $\overline{v^2-f}$ model (CALC-BFC and FLUENT) was obtained. [DOI: 10.1115/1.1929820]

Introduction and Past Studies

An important issue when designing a gas turbine engine is to reduce its influence on the environment. One trend, aiming in this direction, is to use burners designed to produce very low levels of NO_x . The working principle of these low- NO_x burners is to reduce the highest temperatures in the burner rendering a somewhat flatter turbine inlet temperature profile. This trend together with the fact that the performance of the turbine improves with increasing turbine inlet temperature leaves only one option that meets both conditions—distributing hot gas toward the hub and casing (hereafter referred to as end walls). Therefore, it becomes increasingly important to be able to accurately predict the heat transfer rate from the hot gas to the end walls. One flow feature making this rather complicated is the presence of secondary, three-dimensional flow structures, often referred to as horseshoe vortices, which enhance the rate of heat transfer to the endwall.

Previous computations of three-dimensional vane passage flows have in most cases been carried out using different versions of two-equation models for turbulence closure. The most popular ones are the $k-\varepsilon$ and $k-\omega$ models. Ho and Lakshminarayana [1] used the Chien [2] low Reynolds number form of the $k-\varepsilon$ model to compute a vane passage flow experimentally investigated by Gregory-Smith and Cleak [3]. They were able to capture most of the complex flow phenomena in the vicinity of the end wall but never computed any heat transfer data (not measured by [3]). Harvey et al. [4] used an algebraic mixing length model (zero-equation) when they computed end-wall heat transfer rates that were compared to measurements presented in the same paper. The heat transfer rates were claimed to be predicted with an accuracy of $\pm 20\%$ even though the turbulence model used is relatively simple. However, the overall trends in predicted end-wall Nusselt number do not compare very well with measured patterns. An-

other contribution to this area of research is the work performed at NASA Lewis Research Center. For example, Boyle and Jackson [5] computed turbine vane and end-wall heat transfer and compared them to the experiments of Harvey et al. [4]. They investigated the performance of three turbulence models and found differences among the predictions that were greater than the differences in experimental heat transfer between the two configurations computed. Their overall best results were obtained with the Cebeci-Smith turbulence model. More recently Hermanson and Thole [6,7] computed the flow measured by, e.g., Radomsky and Thole [8] using different turbulence models available in FLUENT. Here they investigated the influence of inlet conditions and Mach number on the end-wall secondary flow. Later Hermanson et al. [9] computed the same flow using the $\overline{v^2-f}$ model implemented in FLUENT. Rather good agreement with measurements, both in terms of mean flow and heat transfer, was reported. Another example of promising results using the $\overline{v^2-f}$ model in complex three-dimensional boundary layer flows was presented by Parneix et al. [10] who successfully computed the horseshoe vortex around a wall-mounted appendage.

The $\overline{v^2-f}$ turbulence model, originally suggested by Durbin (e.g., [11]) has, during the last few years, become increasingly popular because of its ability to account for near-wall damping without use of ad hoc damping functions. In this work the performance of two versions of this model will be assessed by computing the flow field in the scaled-up stator vane passage investigated by Kang and Thole [12]. Two codes, the commercial package FLUENT and the in-house code CALC-BFC will be compared by computing exactly the same flow field using similar numerical treatments and the same computational mesh.

Governing Equations

Mean Flow Equations. The steady RANS equations read

$$U_j \frac{\partial U_i}{\partial x_j} = -\frac{1}{\rho} \frac{\partial P}{\partial x_i} + \nu \frac{\partial^2 U_i}{\partial x_j^2} - \frac{\partial}{\partial x_j} \overline{u_i u_j}, \quad \frac{\partial U_j}{\partial x_j} = 0 \quad (1)$$

¹To whom correspondence should be addressed.

Contributed by the Turbomachinery Division of THE AMERICAN SOCIETY OF MECHANICAL ENGINEERS for publication in the JOURNAL OF TURBOMACHINERY. Manuscript received May 17, 2004; revised manuscript received January 13, 2005. Editor: D. Wisler.

Table 1 $\overline{v^2}$ - f model constants

Model	C_μ	$C_{\epsilon d}$	$C_{\epsilon 2}$	C_1	C_2	σ_k	σ_ϵ	C_L	C_η
1	0.22	0.045	1.9	1.4	0.3	1.0	1.3	0.25	85
2	0.19	0.045	1.9	0.4	0.3	1.0	1.3	0.23	70

$$U_i \frac{\partial T}{\partial x_i} = \frac{\partial}{\partial x_i} \left(\frac{\nu}{Pr} \frac{\partial T}{\partial x_i} - u_i t \right) \quad (2)$$

Turbulence Closure. The unknown Reynolds stresses and turbulent heat fluxes are closed using the eddy-viscosity concept, i.e.,

$$\overline{u_i u_j} = -2\nu_t S_{ij} + \frac{2}{3} k \delta_{ij}; \quad \overline{u_i t} = -\frac{\nu_t}{\sigma_t} \frac{\partial T}{\partial x_i} \quad (3)$$

$$\nu_t = C_\mu \overline{v^2} \mathcal{T}, \quad \text{where } \mathcal{T} = \max \left(\frac{k}{\epsilon}, 6 \sqrt{\frac{\nu}{\epsilon}} \right) \quad (4)$$

The turbulent quantities k and ϵ are governed by

$$u_j \frac{\partial k}{\partial x_j} = \frac{\partial}{\partial x_j} \left[\left(\nu + \frac{\nu_t}{\sigma_k} \right) \frac{\partial k}{\partial x_j} \right] + P_k - \epsilon \quad (5)$$

$$u_j \frac{\partial \epsilon}{\partial x_j} = \frac{\partial}{\partial x_j} \left[\left(\nu + \frac{\nu_t}{\sigma_\epsilon} \right) \frac{\partial \epsilon}{\partial x_j} \right] + \frac{C_{\epsilon 1} P_k - C_{\epsilon 2} \epsilon}{\mathcal{T}} \quad (6)$$

In this work two different $\overline{v^2}$ - f models have been used. They will hereafter be referred to as model 1 and model 2, respectively. In model 1, given in Parneix et al. [10], the wall-normal Reynolds stress component, $\overline{v^2}$, is modeled using

$$u_j \frac{\partial \overline{v^2}}{\partial x_j} = \frac{\partial}{\partial x_j} \left[\left(\nu + \frac{\nu_t}{\sigma_k} \right) \frac{\partial \overline{v^2}}{\partial x_j} \right] + k f - \frac{\overline{v^2}}{k} \epsilon \quad (7)$$

$$L^2 \frac{\partial^2 f}{\partial x_j^2} - f = \frac{C_1 - 1}{\mathcal{T}} \left(\frac{\overline{v^2}}{k} - \frac{2}{3} \right) - C_2 \frac{P_k}{k} \quad (8)$$

The turbulent length scale L and the modified coefficient $C_{\epsilon 1}$ are calculated using

$$L = C_L \max \left(\frac{k^{3/2}}{\epsilon}, C_\eta \frac{\nu^{3/4}}{\epsilon^{1/4}} \right), \quad C_{\epsilon 1} = 1.4 \left(1 + C_{\epsilon d} \sqrt{k/\overline{v^2}} \right) \quad (9)$$

The wall boundary conditions for the dissipation rate ϵ and the redistribution parameter f are

$$\epsilon \rightarrow 2\nu \left(\frac{k}{y^2} \right); \quad f \rightarrow -\frac{20\nu^2}{\epsilon} \left(\frac{\overline{v^2}}{y^4} \right) \text{ as } y \rightarrow 0 \quad (10)$$

These boundary conditions (especially that for f) make the original formulation numerically unstable. Therefore a redefinition of f has been proposed in order to have $f=0$ on walls. This modification, used in, e.g., Kalitzin [13] and Lien and Kalitzin [14], renders the following $\overline{v^2}$ and f equations (model 2)

$$u_j \frac{\partial \overline{v^2}}{\partial x_j} = \frac{\partial}{\partial x_j} \left[\left(\nu + \frac{\nu_t}{\sigma_k} \right) \frac{\partial \overline{v^2}}{\partial x_j} \right] + k f - 6\overline{v^2} \frac{\epsilon}{k} \quad (11)$$

$$L^2 \frac{\partial^2 f}{\partial x_j^2} - f = \frac{C_1}{\mathcal{T}} \left(\frac{\overline{v^2}}{k} - \frac{2}{3} \right) - C_2 \frac{P_k}{k} - 5 \frac{\overline{v^2}}{k \mathcal{T}} \quad (12)$$

Note that the models given in Lien and Kalitzin [14] and Kalitzin [13] only differ in model constant values. For a more thorough discussion on the differences between the above models, see [15]. Finally, the turbulence model constants of models 1 and 2 are shown in Table 1.

The Realizability Constraint. Most eddy-viscosity-based turbulence models overpredict the turbulent kinetic energy k in stag-

nation point flows. Durbin [16] suggested a bound on the turbulent time scale \mathcal{T} derived from $2k \geq \overline{u^2} \geq 0$, which significantly improves predictions of k . For $\overline{v^2}$ - f models this constraint implies

$$\mathcal{T} = \min \left[\max \left(\frac{k}{\epsilon}, 6 \sqrt{\frac{\nu}{\epsilon}} \right), \frac{C_{\text{lim}} k}{3 C_\mu \overline{v^2} \max \lambda_\alpha} \right] \quad (13)$$

where the constant C_{lim} has been added to allow for tuning against experiments and $\max \lambda_\alpha$ is the largest eigenvalue of the strain rate tensor S_{ij} . In this work C_{lim} is set to 0.6, which is the most commonly used value. The mechanism responsible for the improvement in k predictions is the reduction in modeled production rate of k . For further discussion on this subject, see [17].

Numerical Considerations and Test Case

The in-house code CALC-BFC is a structured code using SIMPLEC and a colocated grid arrangement with Rhie and Chow interpolation. The van Leer scheme (a bounded, second order upwind scheme) was used when discretizing both momentum and turbulence equations. The resulting set of equations were solved with either a segregated or a coupled tridiagonal matrix solver (TDMA). In the coupled solver the k - ϵ equations and/or the $\overline{v^2}$ - f equations were solved in a coupled manner [15]. Whenever the commercial software FLUENT was used for comparison with CALC-BFC results, efforts were made to keep all numerical features similar to those described above. The $\overline{v^2}$ - f version used in FLUENT was a trial version for FLUENT 5 implemented using user-defined functions.

The three-dimensional experimental test case used for validation is the low-turbulence intensity case ($Tu_{\text{inl}}=0.6\%$) documented in Kang and Thole [12]. The heat fluxes were measured by attaching a constant heat flux film to the end wall, the film-covering locations downstream $x/C=-0.475$. This film is cooled by the passage flow and by measuring the heat flux film temperature the heat transfer coefficient can be determined. For a detailed description of the experiments, see [12]. In Fig. 1 a slice of the computational domain is shown. The inlet is located 1C upstream

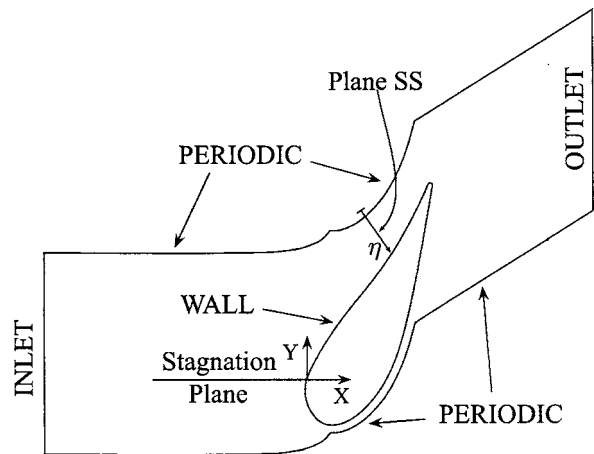


Fig. 1 Computational domain and the location of the stagnation plane and the plane SS that will be used for plotting. When the coordinate η is used $\eta=0$ is located on the suction side, $\eta=1$ on the pressure side.

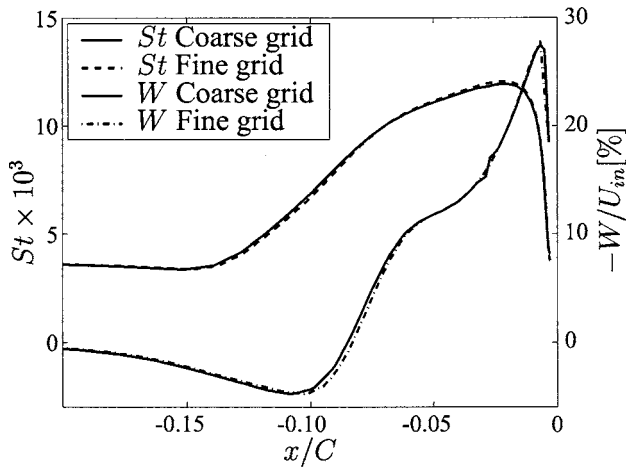


Fig. 2 End-wall Stanton number along the stagnation line ($Y=0$) and spanwise velocity along a line crossing the center of the horseshoe vortex roll-up ($Y=0, Z=0.014S$)

the leading edge (chord $C=0.594$ m, pitch $P=0.77C$, span $S=0.93C$). The end wall is treated as a constant heat flux wall for $x/C \geq -0.475$, otherwise adiabatic. The vane wall is also modeled as being adiabatic. At midspan a symmetry boundary condition is used. At the inlet a measured velocity profile was specified. The inlet turbulence quantities were not available (except at midspan) but were obtained from a separate computation based on the given velocity profile and the assumption that the turbulence field was fully developed. The sensitivity to these boundary conditions are investigated. All fluid properties are assumed to be independent of temperature variations. The mesh consists of an O grid around the vane and three additional blocks, one located upstream of the vane, one downstream and one in the vane passage. The total number of cells for the standard mesh was 650,000. In the end-wall stagnation region y^+ values were <0.5 and all around the vane $y^+ < 2$. In order to investigate grid sensitivity, a finer mesh, 1.8 M nodes, was created. Some results of the grid dependency study are shown in Fig. 2. Here \bar{v}^2-f model 2 predictions of the end-wall Stanton number along the stagnation line are shown for the two meshes together with the secondary (spanwise) velocity component along a line crossing the center of the horseshoe vortex roll-up. Both profiles suggest that the results are grid independent and the coarser mesh was used for most computations. The momentum equations were assumed to be fully converged when the residuals scaled with $\dot{m}U_{in}$ were $<10^{-3}$.

2D Flow Field Results

In order to illustrate the importance of the realizability constraint contours of k/U_{in}^2 for the stator vane flow are shown in Fig. 3. In both cases \bar{v}^2-f model 1 was used with the only difference that in the left figure the realizability constraint, Eq. (13), is deactivated. It can be seen that the constraint has a strong influence. For example, when the limiter is active, it is only in a region around the wake that k/U_{in}^2 exceeds levels of 10^{-3} , whereas the same quantity is well above this value in almost the entire domain if the constraint is not used.

In Fig. 4 predictions of stator vane Stanton number are compared to measurements for some \bar{v}^2-f model 1 computations. Two cases with different inlet turbulence levels are computed. In the region around the stagnation point and along the pressure side of the vane the results agree well with experimental data both for the high ($Tu=10\%$) and low ($Tu=0.6\%$) turbulence intensity case. On the suction side, transition is predicted far too early, which has a strong impact on the heat transfer. Also included in this figure are the results of \bar{v}^2-f model 1 for the low-turbulence

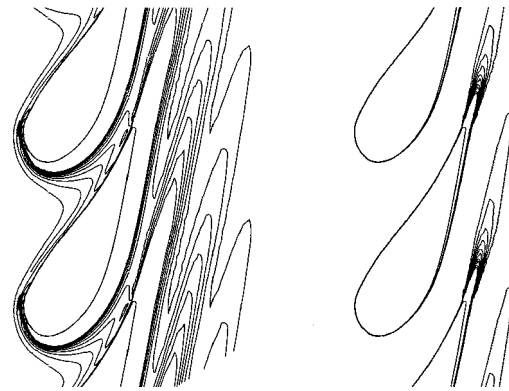


Fig. 3 Contours of k/U_{in}^2 . Inlet FBW from left. Left: \bar{v}^2-f Model 1 without realizability constraint; Right: As left but with realizability constraint. Contour intervals of 0.001.

intensity case where the realizability constraint has not been used. When the constraint is deactivated the predicted heat transfer on the pressure side is almost as high as for the $Tu=10\%$ case. The results are even worse on the suction side. Worth mentioning is that the \bar{v}^2-f model does well in capturing the increase in heat transfer close to the pressure side trailing edge where most eddy-viscosity-based turbulence models usually fail. As an example results of the realizable $k-\epsilon$ model are included showing too a high increase in Stanton number along the pressure side. The \bar{v}^2-f model 1 and the Realizable $k-\epsilon$ model results agree well (especially the former) with results presented by Hermanson et al. [9], who used the FLUENT version of \bar{v}^2-f model 2.

Three-Dimensional Flow Field Results

In this section results of three-dimensional computations of the stator vane flow field will be presented. Most of the results are presented as either contour or vector plots in two different planes—the stagnation plane and a plane labeled SS located some distance into the vane passage. The location of the planes are shown in Fig. 1 together with a coordinate η ranging from 0 to 1, $\eta=0$ being the suction side and $\eta=1$ the pressure side.

Stagnation Region Flow Field. One of the most interesting regions of the flow field in a stator vane passage is the flow in the stagnation region. Here the main flow is retarded by the presence of the vane, and the vorticity in the in-coming boundary layer is

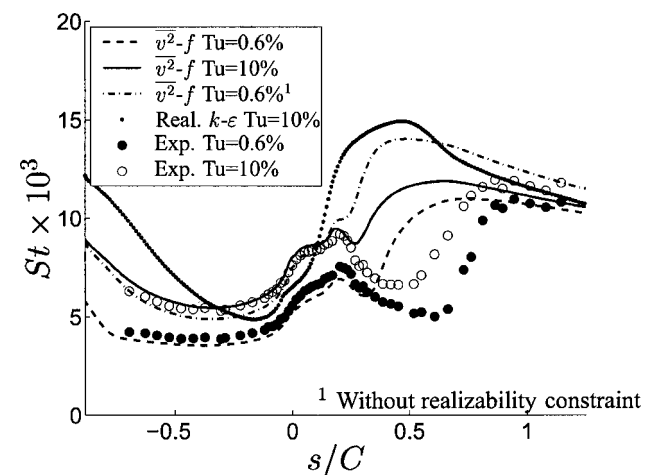


Fig. 4 Measured and predicted (\bar{v}^2-f model 1 and realizable $k-\epsilon$ model) Stanton number along the midspan of the vane. $s/C \geq 0$: suction side. $s/C \leq 0$: pressure side.

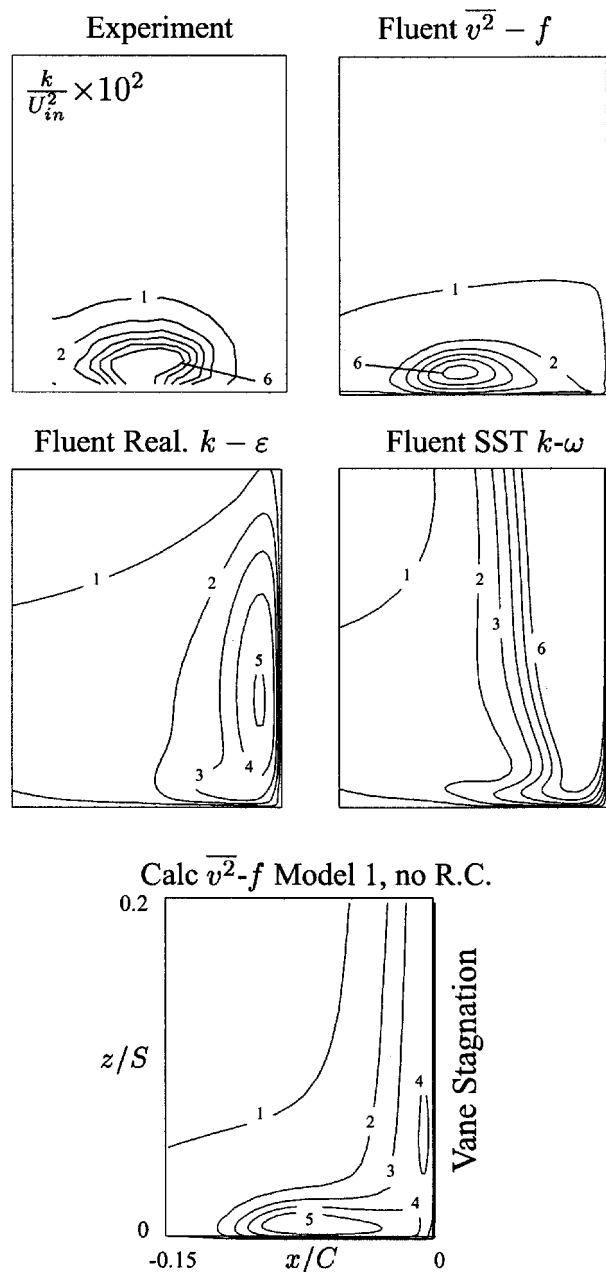


Fig. 5 Contours of $k/U_{in}^2 \times 10^2$ in the stagnation plane (contour interval of $0.01k/U_{in}^2$)

transformed into a so-called horseshoe vortex system. As will be illustrated later, capturing this secondary motion is important when determining the heat transfer to the end walls.

In this work the performance of the different turbulence models is investigated. The only difference between the models that affects the mean flow field will be found in the estimates of the eddy viscosity ν_t . One important flow variable in the expression for ν_t is the turbulence kinetic energy k . In Fig. 5 contours of k in the stagnation plane are shown for four different computations. The differences among the predictions are striking. For example, the peak in k coinciding with the horseshoe vortex center is correctly captured by the $\overline{v^2}-f$ model (both with and without use of the realizability constraint). With the realizable $k-\epsilon$ model a peak in k is erroneously located along the vane stagnation line, whereas with the shear stress transport (SST) $k-\omega$ model the problem of overpredicting the growth of turbulence energy in stagnation point flows has not been solved. Note that Menter [18] suggested a

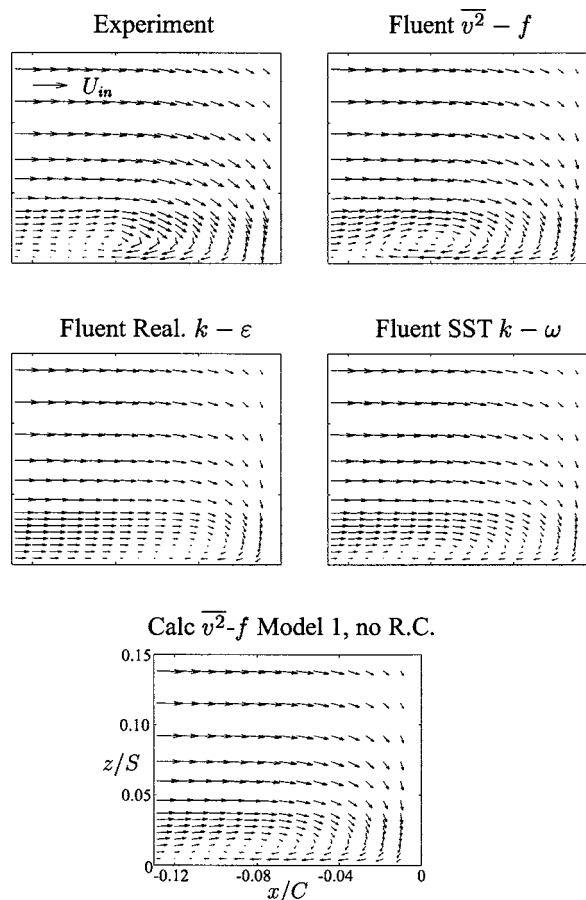


Fig. 6 Velocity vectors in the stagnation plane showing the horseshoe vortex roll-up

limiter on the production term in the k equation of the SST model that addresses this problem. However, this limiter is obviously not implemented in the FLUENT version of the SST model. Also note that the growth problem is present also in the $\overline{v^2}-f$ computation where the realizability constraint is not used. Also note that it can be seen that the FLUENT $\overline{v^2}-f$ model prediction of k agrees well with measured data, both qualitatively and quantitatively (almost identical profiles were obtained with both $\overline{v^2}-f$ models implemented in CALC-BFC when the realizability constraint was used).

In Fig. 6 the computed velocity vectors in the stagnation plane are compared to measured velocities. It can be seen that both the location of the horseshoe vortex and its intensity is accurately predicted by the $\overline{v^2}-f$ model (predicted vortex center: $-0.0825x/C$, $0.0165z/S$, measured vortex center: $-0.083x/C$, $0.016z/S$). The intensity of the horseshoe vortex roll-up predicted by the realizable $k-\epsilon$ and SST $k-\omega$ models are substantially weaker, the former not being able to reproduce a vortexlike signature. This is because of too a large growth of predicted eddy viscosity (which is closely related to k) having the effect that the recirculating motion in this region is restrained by turbulence momentum transport. By comparison with the k profiles in Fig. 5 these results are somewhat surprising. For example, the SST $k-\omega$ model, which suffers from the stagnation point anomaly, predicts a stronger secondary motion than the realizable $k-\epsilon$ model does. Furthermore, the realizable $k-\epsilon$ and the $\overline{v^2}-f$ model k profiles are equal in magnitude, but the former fails almost completely in predicting the vortex roll-up. Also note that the differences in k of the two $\overline{v^2}-f$ models has only little effect on the stagnation region mean flow field. Although not shown here, the realizability constraint has an even stronger effect on ν_t

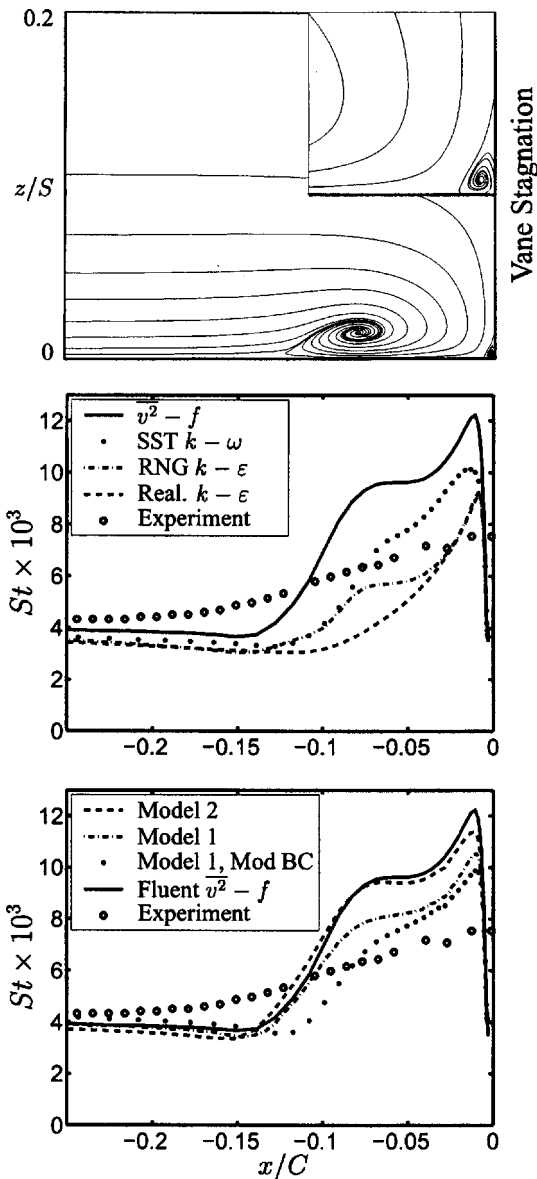


Fig. 7 Top: Streamlines of FLUENT \bar{v}^2-f computation illustrating the horseshoe and leading-edge corner vortices in the stagnation plane. Middle: Measured and predicted (FLUENT) Stanton number along the end-wall stagnation line. Bottom: CALC-BFC predictions.

than on k . In this flow the constraint is activated (cf. Eq. (13)) just downstream of the inlet and as the flow reaches the vane stagnation the inlet eddy viscosity has been reduced by more than 90%. Because of the large difference in ν_t it is a surprise that mean flow fields (top right and bottom in Fig. 6) are nearly the same. However, as was seen in Fig. 4, the predicted heat fluxes were strongly influenced when the constraint was switched off. The reason why the mean flow field is less sensitive to ν_t in the stagnation region is the presence of a strong pressure gradient. This pressure gradient outweighs to some extent the effect of the poorly predicted Reynolds stresses in the mean flow equations but it does not enter the energy equation. Thus, the effects of an inaccurate prediction of ν_t is often greater on heat transfer than on momentum transfer.

Another interesting feature of the stagnation region flow is illustrated in Fig. 7 (top figure). Here particle traces (restricted to a plane) in the stagnation plane are shown. The large horseshoe vortex structure is easily identified. In a close-up of the stator vane/endwall junction another much smaller (about 0.01 chord

wide) counterrotating vortex is also shown. This vortex was postulated by Goldstein and Spores [19] who observed a small region of very high local heat transfer at the abovementioned junction. Later Wang et al. [20] verified its existence with detailed flow field measurements. Note that the measured velocity vectors in Fig. 6 also indicate the presence of this vortex. A possible attachment point can be seen (last row of vectors) but the resolution is not fine enough to visualize the vortex.

Stagnation Region Heat Transfer. In the preceding section some characteristics of the mean flow field were investigated. Another important issue is how the heat transfer to the end wall is affected by the presence of the horseshoe vortex. If this vortex is strong, then it will tear up the incoming, insulating boundary layer and replace the relatively cold fluid close to the end wall with hot gas from the free-stream region. An example of this phenomenon is seen in Fig. 7 (top) where the flow is directed downward in between the center of the horseshoe vortex and the stator vane. In order to illustrate the influence this has on heat transfer, the predicted Stanton number along the end-wall stagnation line is plotted in Fig. 7 (middle) for the FLUENT computations.

Two important conclusions can immediately be drawn. The end-wall heat transfer in the region well upstream of the stator vane is fairly accurately predicted with Stanton numbers some 10–15% too low, independent of choice of turbulence model. The slight undershoot is probably due to the inlet boundary layer profiles of the turbulent quantities not being fully consistent with the experimental setup. Unfortunately, the experimental inlet profiles of k and \bar{v}^2 needed to verify this are not available. Second, the heat transfer in the region of the horseshoe vortex roll-up seems to be fairly independent of the inlet conditions. Instead it is determined by the intensity of the vortex itself, which is in line with the above discussion on hot and cold gas exchange. Therefore the \bar{v}^2-f model, which predicts the strongest secondary motion, also gives the highest rates of heat transfer. In this case the FLUENT \bar{v}^2-f model overpredicts the Stanton number by $\sim 50\%$ in the stagnation region. Here the SST $k-\omega$ and the renormalization group (RNG) $k-\varepsilon$ models agree the best with measurements. This is unexpected as both models underpredict the roll-up of the horseshoe vortex, which is the flow feature responsible for the stagnation region increase in heat transfer. Also note the peaks in heat transfer close to the end-wall and/or stator vane junction. At this location, between the horseshoe and the leading-edge corner vortices, the free-stream flow attaches to the end wall and a new, initially very thin, boundary layer begins to develop. This feature is absent in the experiments, which is due to either insufficient resolution or the mean flow not being stationary.

In Fig. 7 (bottom figure) the corresponding results from three different CALC-BFC \bar{v}^2-f computations are shown (also included for reference is the FLUENT \bar{v}^2-f computation). It can be seen that the highest heat transfer rates are predicted by the FLUENT model and \bar{v}^2-f model 2. These results being almost identical suggests that the two models and their implementations in the two different codes are very similar. The \bar{v}^2-f model 1 results agree rather well with measurements in the vortex dominated region and as this model in large also captures the intensity of the secondary motion it is regarded to produce the best overall agreement with measurements. In order to investigate the possible influence of the prescribed inlet boundary conditions for the turbulent quantities one additional Model-1 computation was added. Here the inlet k profile was kept the same whereas the ε and \bar{v}^2 were specified according to

$$\varepsilon = C_\mu \frac{k^{3/2}}{L}, \quad \bar{v}^2 = \frac{2}{3}k \quad (14)$$

where L (here the measured $L=0.09$ m was used) is a characteristic turbulence length scale. As can be seen this change has some influence on the location of the horseshoe vortex and has also increased the heat transfer upstream the vortex by a few percent.

Worth mentioning is that several inlet boundary conditions were tried (constant profiles corresponding to different levels of turbulence intensity) of which the one reported here had the greatest impact on the results. The conclusion is that the end-wall heat transfer in the stagnation region is not very sensitive to the specified inlet boundary conditions. Thus it is neither expected to be sensitive to the inlet *level* of turbulence intensity, but rather to how well the roll-up of the horseshoe vortex is captured. This trend has also been seen in experiments by Radomsky and Thole [8].

The effect of the realizability constraint on the end-wall stagnation region heat transfer was rather small (not shown here). This finding is supported by the fact that the k profiles along the end wall obtained with and without the constraint are alike (cf. Fig. 5) and that the predicted secondary motions, which are of greater importance, are almost identical. Finally, note that the Stanton number signature of the horseshoe vortex is not as detailed in the experiments as in the computations. This can have only two explanations: (i) The vortex is not completely stationary but moves in the streamwise direction. This phenomenon cannot be captured in steady computations (model error). (ii) The measured end-wall temperature is influenced by heat conduction within the constant heat flux film (experimental uncertainty). Both these phenomena would smear out the time-averaged Stanton profile.

Secondary Velocities Between Two Vanes. In order to visualize the horseshoe vortices emanating from the vane-end-wall junction secondary velocities (the total local velocity minus the local velocity in the midspan flow direction, see [12] for further details) are plotted in Fig. 8 for plane SS (cf. Fig. 1). As the intensity of the secondary motion is concentrated towards the end wall only one quarter of full passage is included ($0 < z/S < 0.25$).

In both the experiments and the computations, two secondary structures are visible. The structure to the left is the suction-side leg of the horseshoe vortex, whereas the right structure is the motion resulting from effects of the pressure-side leg of this vortex and the passage vortex. The center locations of the vortices in this plane predicted with the $\overline{v^2}-f$ model agree fairly well with the experiment, both lying slightly too close to their respective stator wall. The strength of the vortices, especially the lower part of the passage vortex, however, is underpredicted. The reason why the secondary motion in this region is strong is that the low streamwise momentum fluid in the end-wall boundary layer is being sucked toward the suction side of the adjacent vane. Fluid higher up in the passage (at higher z/S) has higher streamwise velocity magnitude (momentum) and is therefore not as strongly affected by this pressure difference between the vanes. This “passage-vortex” effect is one of the flow features that is not very well captured in the computations.

In order to illustrate the coupling between the secondary motion and the end-wall heat transfer the Stanton number along the intersection of the end wall and plane SS is shown in Fig. 8. The circles represent measurements in one passage each (here indicating good periodicity of the experiment), whereas the lines are the computed Stanton number of $\overline{v^2}-f$ model 1 and the realizable $k-\varepsilon$ model. In both computations and measurements a peak in heat transfer is located close to the vane suction side. This peak is due to the presence of the suction-side leg of the horseshoe vortex, which distributes hot gas toward the end wall. At this particular location the hot fluid has just reattached to the end wall and the boundary layer is therefore very thin. Toward the pressure side ($\eta=1$) the heat transfer shows a much less distinct increase even though the secondary motion here is stronger. The reason is that the boundary layer here is much thicker than closer to the suction side, i.e., we are well downstream the reattachment location.

With the realizable $k-\varepsilon$ failing to capture the secondary motion, which is important for the heat transfer, it is a surprise that the model gives an almost perfect prediction of the end-wall heat transfer. The authors argue that this is somewhat fortuitous and

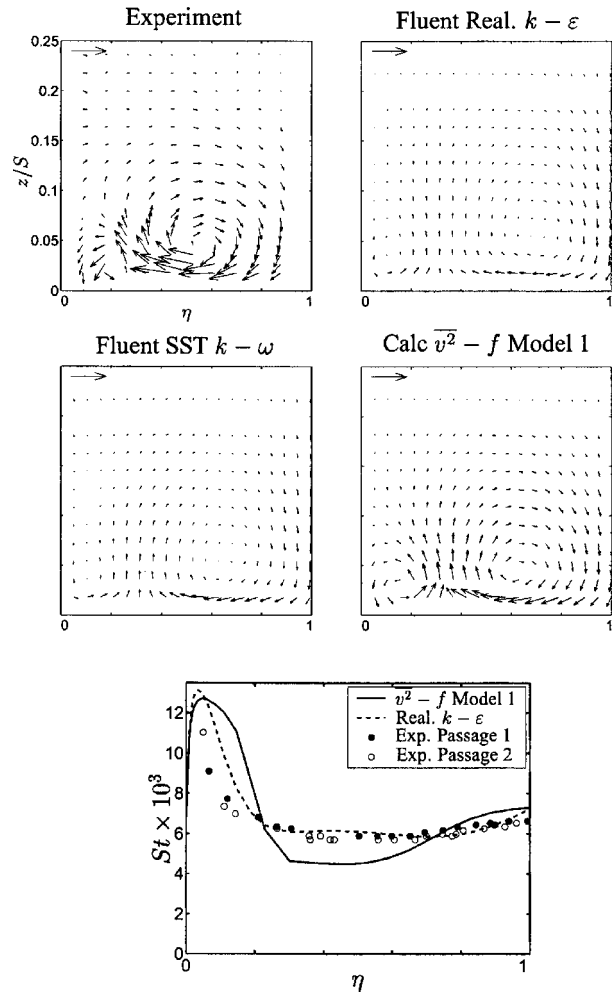


Fig. 8 Predicted secondary velocities in the lower half of plane SS (cf. Fig. 1). The reference arrows correspond to 20% of the maximum total velocity in the plane. Bottom: Endwall Stanton number along the bottom of plane SS.

results not shown here suggests that in the realizable $k-\varepsilon$ computations the predicted thicknesses of the boundary layers are more sensitive to the strong acceleration through the passage than seen in experiment or in any other computation. The $\overline{v^2}-f$ model results agree fairly well with measurements along most of the line but in between the two vortices the heat transfer is underpredicted. As previously mentioned this might be due to the horseshoe vortex not being completely stable in the experiments but moves in the pitchwise direction. A more likely explanation is the too weak predicted motion of low-momentum fluid toward the suction side. In order to illustrate the importance of this flow feature to the end-wall heat transfer some streamlines showing the secondary motion are plotted in Fig. 9. Here streamlines A visualize the very center of the horseshoe vortex pressure leg. Of greater importance are streamlines B. They originate from well above the end wall where the fluid temperature, in general, is high. When these streamlines approach the stator vane they are bent downward by the presence of the horseshoe-passage vortex so that hot fluid is brought in contact with the end wall (this happens along a so-called attachment line) and a new, initially very thin (thermal) boundary layer begins to develop. The extent of this thin boundary layer will have a large influence on the end-wall heat transfer characteristics.

Another effect seen in this figure is that the streamlines B, after having passed plane SS tend to move upward (away from the endwall) along the suction side of the vane due to a spanwise

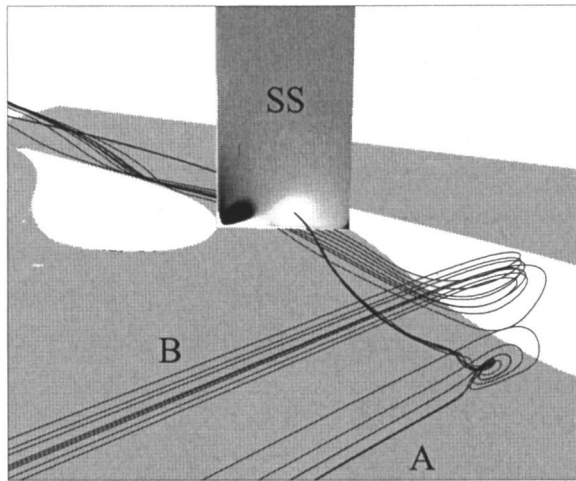


Fig. 9 Streamlines illustrating the secondary fluid motion responsible for the increase in end-wall heat transfer between two stator vanes. Streamlines A indicate the center of the pressure leg of the horseshoe vortex. Streamlines B, entering well above the end wall, are convected downward and spread along the end wall. Plane SS is colored with helicity, light region indicating clockwise rotation (passage vortex), dark region indicating anti-clockwise rotation (suction-side leg of horseshoe vortex).

pressure gradient. Although not shown here they eventually reach a separation line located on the suction side surface. This separation line is due to yet another secondary structure, the leading-edge corner vortex also seen in Fig. 7, that also moves upward along the suction side. In Hermanson et al. [9], the presence of this flow feature was illustrated by plotting the Stanton number on the vane suction side. They found a streak of low heat transfer moving upward along the vane reaching about 15% of the full span at the trailing edge and argued that it was a passage vortex separation line. This is incorrect as the passage vortex lies close to the pressure side of the vane.

Endwall Heat Transfer Between Two Vanes. As shown in preceding sections the computations where the $\overline{v^2}$ - f model has been used to model turbulence effects give the overall best agreement with experiments. Therefore, the *passage* end-wall heat transfer predictions of the different versions of this model will now be compared to measurements. In Fig. 10 the Stanton number along three different lines on the end wall are plotted for a set of $\overline{v^2}$ - f model computations. Included for reference are the results of the realizable k - ϵ model.

At location A the heat transfer is accurately predicted with the exception of the region between the two main vortices mentioned earlier. Again this is due to either an underprediction of the “passage vortex effect,” i.e., the pressure difference between the vanes, or the mean flow not being completely stable. In two of the computations, CALC-BFC model 1 and model 2 with use of the realizability constraint, the peak in Stanton number located near the suction side of the vane is captured to within $\sim 10\%$. Not using the constraint causes an overshoot in this region due to too large turbulent heat fluxes.

At station B the Stanton number predictions indicate that the incoming boundary layer has separated from the end wall along most of the passage, which gives room for the new thinner boundary layer previously mentioned. On the pressure side of the passage ($\eta > 0.4$) CALC-BFC model 1 and model 2 still do a reasonably good job. However, at location B only the model without use of the realizability constraint captures the suction-side peak in heat transfer due to the erroneous overprediction of k . This suggests that the physically correct effect of the suction-side leg of the

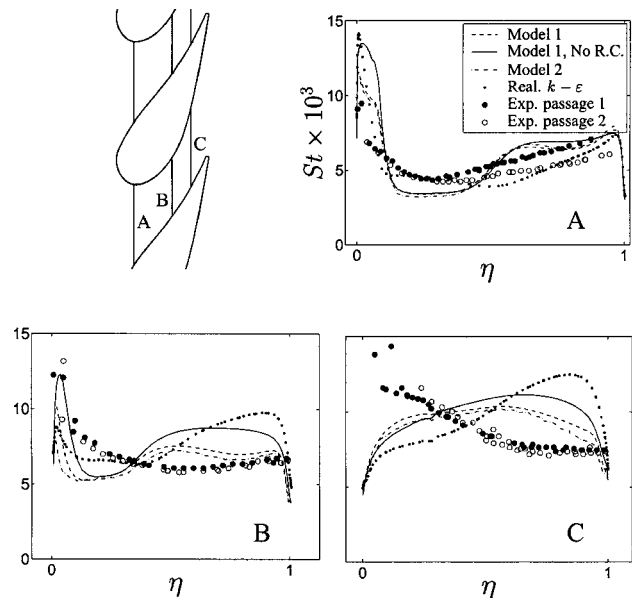


Fig. 10 Stanton number at the end wall along lines A-C

horseshoe vortex on end-wall heat transfer is underpredicted. Further into the passage, at station C, this deficiency of the computations is even more obvious as all models fail to capture the trend of increasingly higher heat transfer at the suction side of the passage. At this location the predictions towards the pressure side also begin to seriously deviate from the measured values.

The mismatch at the suction side can no longer be explained by the underprediction of the extent of the thin boundary layer. Instead this is probably due to the intensity of the predicted suction-side leg of the horseshoe vortex being too weak. Another possible explanation is, as the flow turning angle is large, that effect of curvature on the turbulence play an important role. A correct representation of streamline curvature require more sophisticated turbulence closures than standard eddy-viscosity models offer (e.g., Reynolds stress models). Also note that as we move into the passage it becomes increasingly more difficult to explain local differences between experiments and computations by investigating local quantities due to accumulation of upstream, “history” effects. For example, it was found that the secondary motion toward the suction side was not very well captured. The adding up of that effect will most likely influence the heat transfer characteristics some distance into the passage.

Conclusions

The performance of the $\overline{v^2}$ - f turbulence model has been assessed by computing a three-dimensional stator vane flow with complex secondary structures present. The results of two versions of this model were compared to detailed measurements of the mean flow, turbulence quantities, and heat transfer. Comparison was also made to other eddy-viscosity-based turbulence models available in FLUENT, including a version of the $\overline{v^2}$ - f model. It has been shown that the flow feature that in large determines the end-wall heat transfer in the stagnation region is the roll-up of a secondary vortex system. This has earlier been seen in experiments and in this work the mechanism behind this coupling of secondary flow and end-wall heat transfer has been illustrated. It was found that the predictions that in general agreed the best with experimental data were those computed using the $\overline{v^2}$ - f model for turbulence closure. However, also this model to some extent underpredicts the intensity of the secondary motion, which has the consequence that the endwall heat transfer characteristics is sometimes not captured. Furthermore, the importance of preventing unphysical growth of turbulence kinetic energy, here by use of a

realizability constraint, was illustrated. Very good agreement between the implementations of $\overline{v^2-f}$ model 2 in CALC-BFC (in-house code) and FLUENT (commercial code) was obtained in terms of both secondary flow fields and end-wall heat transfer. Finally, of the different versions of the $\overline{v^2-f}$ model investigated, model 1, a model very similar to that originally suggested by Durbin [21], gave the overall best agreement with experimental data.

Acknowledgment

The present work was supported by the Swedish Gas Turbine Center. The authors would also like to acknowledge Prof. K. A. Thole for supplying experimental data.

Nomenclature

- C = true vane chord
 C_{lim} = constant in the realizability constraint
 H = helicity, $H = \omega_i U_i$
 h = heat transfer coefficient, $h \equiv q_{wall} / (T_{wall} - T_{in})$
 L = turbulent length scale
 P = vane pitch
 S = vane span; $S^2 = S_{ij} S_{ij}$
 S_{ij} = strain rate tensor, $S_{ij} \equiv \frac{1}{2} (\partial U_i / \partial x_j + \partial U_j / \partial x_i)$
 St = Stanton number, $St \equiv h / \rho C_p U_{in}$
 \mathcal{T} = turbulent time scale
 $\overline{u_i u_j}$ = Reynolds stress tensor
 $\overline{v^2}$ = normal stress in the wall-normal direction

References

- [1] Ho, Y.-H., and Lakshminarayana, B., 1996, "Computational Modelling of Three-Dimensional Endwall Fbw Through a Turbine Rotor Cascade With Strong Secondary Fbws," *J. Turbomach.* **118**, 250-261.
 [2] Chien, K. Y., 1982, "Predictions of Channel and Boundary Layer Flows With a Low Reynolds Number Turbulence Model," *AIAA J.* **20**, pp. 33-38.
 [3] Gregory-Smith, D., and Cleak, J., 1992, "Secondary Fbw Measurements in a Turbine Cascade With High Inlet Turbulence," *J. Turbomach.* **114**, 173-183.
 [4] Harvey, N., Rose, M., Coupland, J., and Jones, T., 1999, "Measurement and

- Calculation of Nozzle Guide Vane End Wall Heat Transfer," *J. Turbomach.* **121**, 184-190.
 [5] Boyle, R., and Jackson, R., 1997, "Heat Transfer Predictions for Two Turbine Nozzle Geometries at High Reynolds and Mach Numbers," *J. Turbomach.* **119**, 270-283.
 [6] Hermanson, K., and Thole, K., 2000, "Effect of Inlet Conditions on Endwall Secondary Fbws," *J. Propul. Power* **16**, 286-296.
 [7] Hermanson, K., and Thole, K., 2000, "Effect of Mach Number on Secondary Fbw Characteristics," *International Journal of Turbo and Jet Engines* **17**, 179-196.
 [8] Radomsky, R., and Thole, K., 2000, "High Free-Stream Turbulence Effects on Endwall Heat Transfer for a Gas Turbine Stator Vane," *J. Turbomach.* **122**, 699-708.
 [9] Hermanson, K., Kern, S., Picker, G., and Parneix, S., 2003, "Predictions of External Heat Transfer for Turbine Vanes and Blades With Secondary Fbw-fields," *J. Turbomach.* **125**, 107-113.
 [10] Parneix, S., Durbin, P., and Behnia, M., 1998, "Computation of 3-D Turbulent Boundary Layers Using the V2F Model," *Flow, Turbul. Combust.* **60**, 19-46.
 [11] Durbin, P., 1991, "Near-Wall Turbulence Closure Modeling Without "damping functions"," *Theor. Comput. Fluid Dyn.*, **3**, 1-13.
 [12] Kang, M., and Thole, K., 2000, "Flowfield Measurements in the Endwall Region of a Stator Vane," *J. Turbomach.* **122**, 458-466.
 [13] Kalitzin, G., 1999, "Application of the $\overline{v^2-f}$ Model to Aerospace Configurations," Center for Turbulence Research Annual Research Briefs.
 [14] Lien, F., and Kalitzin, G., 2001, "Computations of Transonic Fbw With the $\overline{v^2-f}$ Turbulence model," *Int. J. Heat Fluid Flow* **22**, 53-61.
 [15] Sveningsson, A., 2003, "Analysis of the Performance of Different $\overline{v^2-f}$ Turbulence Models in a Stator Vane Passage Fbw," Licentiate thesis, Dept. of Thermo and Fluid Dynamics, Chalmers University of Technology, Gothenburg, Sweden.
 [16] Durbin, P., 1995, "On the $k-3$ Stagnation Point Anomaly," *Int. J. Heat Fluid Flow* **17**, 89-90.
 [17] Sveningsson, A., and Davidson, L., 2003, "Assessment of Realizability Constraints and Boundary Conditions in $\overline{v^2-f}$ Turbulence Models," 4th Int. Symp. on Turbulence Heat and Mass Transfer, Antalya, Turkey.
 [18] Menter, F., 1993, "Zonal Two-Equation $k-\omega$ Turbulence Model for Aerodynamic Fbws," in *AIAA Paper 1993-2906*.
 [19] Goldstein, R., and Spores, R., 1988, "Turbulent Transport on the Endwall in the Region Between Adjacent Turbine Blades," *J. Heat Transfer* **110**, 862-869.
 [20] Wang, H., Olsen, S., Goldstein, R., and Eckert, E., 1997, "Flow Visualisation in a Linear Turbine Cascade of High Performance Turbine Blades," *J. Turbomach.* **119**, 1-8.
 [21] Durbin, P., 1995, "Separated Fbw Computations With the $k-\epsilon-v^2$ Model," *AIAA J.* **33**, 659-664.